

Article

The Microalloying Effect of Ce on the Mechanical Properties of Medium Entropy Bulk Metallic Glass Composites

Yanchun Zhao ^{1,2,*} , Pengbiao Zhao ², Wensheng Li ^{1,2,*}, Shengzhong Kou ^{1,2}, Jianlong Jiang ², Xuejing Mao ² and Zhuang Yang ²

¹ State Key Laboratory of Advanced Processing and Recycling of Non-ferrous Metals, Lanzhou University of Technology, Lanzhou 730050, China; kousz@lut.cn

² Department of Materials Science and Engineering, Lanzhou University of Technology, Lanzhou 730050, China; 172080503013@lut.edu.cn (P.Z.); 162080503068@lut.edu.cn (J.J.); 172080503046@lut.edu.cn (X.M.); 1701050263@lut.edu.cn (Z.Y.)

* Correspondence: zhaoyanchun@lut.edu.cn (Y.Z.); liws@lut.edu.cn (W.L.)

Received: 3 September 2019; Accepted: 12 September 2019; Published: 15 September 2019



Abstract: Novel ultra-strong medium entropy bulk metallic glasses composites (BMGCs) $\text{Fe}_{65.4-x}\text{Ce}_x\text{Mn}_{14.3}\text{Si}_{9.4}\text{Cr}_{10}\text{C}_{0.9}$ and $\text{Ti}_{40-x}\text{Ce}_x\text{Ni}_{40}\text{Cu}_{20}$ ($x = 0, 1.0$), through the martensite transformation induced plasticity (TRIP effect) to enhance both the ductility and work-hardening capability, were fabricated using magnetic levitation melting and copper mold suction via high frequency induction heating. Furthermore, the Ce microalloying effects on microstructure and mechanical behaviors were studied. The Fe-based BMGCs consisted of face-centered cubic (fcc) γ -Fe and body-centered cubic (bcc) α -Fe phase, as well as Ti-based BMGCs containing supercooled B2-Ti (Ni, Cu) and a thermally induced martensite phase B19'-Ti (Ni, Cu). As loading, the TRIP BMGCs exhibited work-hardening behavior, a high fracture strength, and large plasticity, which was attributed to the stress-induced transformation of ε -Fe martensite and B19'-Ti (Ni, Cu) martensite. Ce addition further improved the strengthening and toughening effects of TRIP BMGCs. Adding elemental Ce enhanced the mixing entropy ΔS_{mix} and atomic size difference δ , while reducing the mixing enthalpy ΔH_{mix} , thus improving the glass forming ability and delaying the phase transition process, and hence prolonging the work-hardening period before fracturing. The fracture strength σ_f and plastic stress ε_p of $\text{Ti}_{39}\text{CeNi}_{40}\text{Cu}_{20}$ and $\text{Fe}_{64.4}\text{CeMn}_{14.3}\text{Si}_{9.4}\text{Cr}_{10}\text{C}_{0.9}$ alloys were up to 2635 MPa and 13.8%, and 2905 MPa and 30.1%, respectively.

Keywords: bulk metallic glass composites; martensitic phase transformation; mechanical property

1. Introduction

Due to their special structural properties of short-range order and long-range disorder, bulk metallic glasses (BMGs) exhibit excellent mechanical and functional properties, such as a high strength and elastic limit, low elastic modulus, and excellent wear-corrosion resistance [1,2]. However, a fatal drawback of BMGs, the limited ductility and strain softening as loading, restricts its application as an advanced structural material [3–5]. Recently, some alloy systems have offered the possibility to produce in situ composites consisting of shape memory crystals and a glassy matrix [6–9]. Bulk metallic glass composites (BMGCs) can overcome the problems with BMGs using a transformation induced plasticity (TRIP) effect as loading [10–13]. Besides, in recent years, it has been found that the addition of rare earth elements can not only effectively improve the ability of amorphous formation, but also play an important role toward deoxidation, metamorphism, and strengthening alloys [14,15]. As Ce is the most

abundant rare earth element, being easy to extract and of low cost, it has become the preferred choice for research and industrial application [16]. In the current work, we developed Fe-based and Ti-based TRIP BMGCs, which both contain dual crystalline phases besides an amorphous matrix. Furthermore, we discuss the effect of Ce microalloying on the microstructure and work-hardening behaviors of the different alloy systems.

2. Materials and Methods

The ingots of the $\text{Fe}_{65.4-x}\text{Ce}_x\text{Mn}_{14.3}\text{Si}_{9.4}\text{Cr}_{10}\text{C}_{0.9}$ and $\text{Ti}_{40-x}\text{Ce}_x\text{Ni}_{40}\text{Cu}_{20}$ ($x = 0, 1.0$) (atomic percent, at. %) alloys, where $x = 0$ and 1.0 , were prepared by mixing the constituent elements (Trillion Metals Co., Beijing, China) in a vacuum high-frequency induction furnace with a water-cooled Cu crucible under an argon atmosphere. Each ingot was re-melted at least six times to ensure homogeneity. Cylinder samples with a diameter of 2 mm for Fe-based and 3 mm for Ti-based alloys were prepared using suction casting into copper mold. The microstructure of the alloys was studied using an X-ray diffractometer (XRD, D/max-2400, Rigaku Corporation, Tokyo, Japan) with Cu-K α radiation (40 kV, 30 mA), thermal field-emission scanning electron microscopy (SEM, Quanta FEG 450, FEI Co., Hillsboro, Oregon, USA) operated at an acceleration voltage of 10 kV and a working distance of 8 mm, and transmission electron microscopy (TEM, JEM-2010, JEOL Ltd., Tokyo, Japan) coupled with fast Fourier transform (FFT) of the selected area under a 200 kV accelerating voltage. For compression tests, the electronic universal testing machine (Model 3382, Instron Co., Canton, MA, USA) was employed with a strain rate of $5 \times 10^{-4} \text{ s}^{-1}$. The cylinder samples with a height: diameter ratio of 2:1 were fabricated, and both ends of the samples were polished.

3. Results and Discussion

3.1. Microstructure of the Fe-Based and Ti-Based TRIP BMGCs

Figure 1 shows the high-resolution TEM (HRTEM) image and fast Fourier transform (FFT) patterns of selected area for the as-cast $\text{Fe}_{65.4}\text{Mn}_{14.3}\text{Si}_{9.4}\text{Cr}_{10}\text{C}_{0.9}$ and $\text{Ti}_{40}\text{Ni}_{40}\text{Cu}_{20}$ BMGCs, respectively. The disordered atomic arrangement of the amorphous phase, the ordered face-centered cubic γ -austenite, and the body-centered cubic α -ferrite in Fe-based BMGC; and the B2-Ti (Ni, Cu) austenite and B19'-Ti (Ni, Cu) martensite in Ti-based BMGC can be observed.

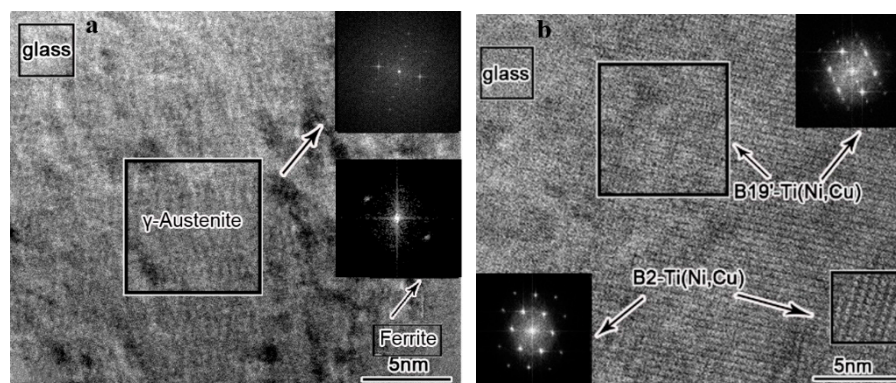


Figure 1. High-resolution transmission electron microscopy (HRTEM) and fast Fourier transform (FFT) of (a) the as-cast $\text{Fe}_{65.4}\text{Mn}_{14.3}\text{Si}_{9.4}\text{Cr}_{10}\text{C}_{0.9}$ and (b) $\text{Ti}_{40}\text{Ni}_{40}\text{Cu}_{20}$ alloys.

Figure 2 gives the X-ray diffraction patterns of as-cast and loading-fracture samples of $\text{Fe}_{65.4-x}\text{Ce}_x\text{Mn}_{14.3}\text{Si}_{9.4}\text{Cr}_{10}\text{C}_{0.9}$ and $\text{Ti}_{40-x}\text{Ce}_x\text{Ni}_{40}\text{Cu}_{20}$ ($x = 0, 1.0$) alloys. Amorphous diffuse scattering peaks can be observed in the XRD patterns of four alloys from $2\theta = 40\text{--}50^\circ$, as well as the crystalline phases that were precipitated and superimposed on the diffuse scattering peaks, verifying that the composites consisted of dual crystal phases and an amorphous matrix. The diffuse scattering peak widths of the as-cast XRD images of $\text{Fe}_{64.4}\text{Ce}_{1.0}\text{Mn}_{14.3}\text{Si}_{9.4}\text{Cr}_{10}\text{C}_{0.9}$ and $\text{Ti}_{39}\text{Ce}_{1.0}\text{Ni}_{40}\text{Cu}_{20}$ alloys with

rare earth element Ce were higher than those without a rare earth element alloy, indicating that the addition of rare earth elements increased the volume fraction of the amorphous phase and enhanced the amorphous forming ability. Meanwhile, the precipitated crystal phases of the two Fe-based as-cast alloys were a supercooled shape memory austenite phase face-centered cubic (fcc) γ -Fe and ferrite phase body-centered cubic (bcc) α -Fe, indicating that both microstructures of the alloys were composed of an amorphous matrix and dual crystalline phases (Figure 2a). The precipitated crystals of the two Ti-based as-cast alloys were confirmed to be supercooled shape memory austenite phase B2-Ti (Ni, Cu) and thermally induced martensite phase B19'-Ti (Ni, Cu) (Figure 2b). As the addition of Ce elements can reduce the temperature of martensitic transformation, the austenite phase was stabilized during solidification. As can be seen from the as-cast XRD patterns, the volume fractions of the γ -Fe and B2-Ti (Ni, Cu) supercooled austenite were more than those of the alloys without the Ce addition. Furthermore, from the XRD patterns of loading fracture samples, the stress-induced hexagonal closed-packed (hcp) ϵ -Fe martensite and the B19'-Ti (Ni, Cu) martensite diffraction peaks can be clearly identified from the as-cast amorphous hump and crystalline peaks. Regarding loading, the local stress increased with the increase of dislocation density in the local region, and ultimately induced the martensite transformation.

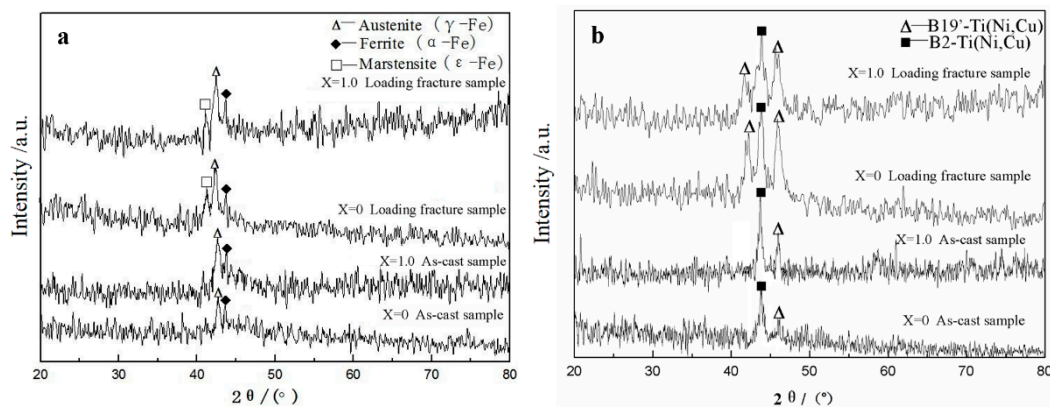


Figure 2. X-ray diffraction patterns of (a) $\text{Fe}_{65.4-x}\text{Ce}_x\text{Mn}_{14.3}\text{Si}_{9.4}\text{Cr}_{10}\text{C}_{0.9}$ and (b) $\text{Ti}_{40-x}\text{Ce}_x\text{Ni}_{40}\text{Cu}_{20}$ ($x = 0, 1.0$) alloys.

The inherent thermodynamic properties dominated the state and properties of the amorphous and crystalline phases. According to Boltzmann's equations [17,18], it is assumed that there are N atoms mixed in an alloy, where n_0, n_1, \dots, n_r are the numbers of different elements and k is the Boltzmann constant; then, the mixing entropy ΔS_{mix} of an alloy is:

$$\Delta S_{\text{mix}} = k \ln\left(\frac{N!}{n_0!n_1!\dots n_r!}\right) \quad (1)$$

When the atomic ratios are non-equal:

$$\Delta S_{\text{mix}} = -R \sum_{i=1}^i x_i \ln x_i \quad (2)$$

where x_i is the atomic percentage of components, and R is the gas constant.

The mixing enthalpy ΔH_{mix} can be calculated by using the mixture enthalpy $\Delta H_{AB}^{\text{mix}}$ of a binary system, which is shown in Table 1 [19]:

$$\Delta H_{\text{mix}} = \sum_{i=1, i \neq j}^N 4\Delta H_{AB}^{\text{mix}} x_i x_j \quad (3)$$

Table 1. ΔH_{AB}^{mix} of the binary elements [20].

Element	Fe	Mn	Si	Cr	C	Ti	Ni	Cu	Ce
Fe		0	−35	−1	−50				3
Mn	0		−45	2	−66				1
Si	−35	−45		−37	−39				−73
Cr	−1	2	−37		−61				15
C	−50	−66	−39	−61					−116
Ti							−35	−9	18
Ni						−35		4	−28
Cu						−9	4		−21
Ce	3	1	−73	15	−116	18	−28	−21	

Thus, ΔS_{mix} and ΔH_{mix} of the four alloys could be calculated using Table 2. All the four TRIP BMGCs were confirmed to be medium entropy materials. Furthermore, the addition of the rare earth element Ce increased ΔS_{mix} , improving the chaos degree of the alloy system, as well as promoting the formation of the denser disordered stacking arrangements. In addition, the reduction of ΔH_{mix} reduced the driving force of crystallization, that is, it improved the amorphous forming ability of the two alloy systems.

Table 2. ΔS_{mix} and ΔH_{mix} of TRIP BMGCs.

Alloy	ΔS_{mix} (J·mol ^{−1} ·K ^{−1})	ΔH_{mix} (kJ·mol ^{−1})	δ (%)
Fe _{65.4} Mn _{14.3} Si _{9.4} Cr ₁₀ C _{0.9}	1.05R	−14.34	3.69
Fe _{64.4} Ce _{1.0} Mn _{14.3} Si _{9.4} Cr ₁₀ C _{0.9}	1.08R	−14.43	5.62
Ti ₄₀ Ni ₄₀ Cu ₂₀	1.06R	−23.72	7.01
Ti ₃₉ Ce _{1.0} Ni ₄₀ Cu ₂₀	1.10R	−24.12	7.85

Moreover, the parameter Ω , which can combine the effects of ΔS_{mix} and ΔH_{mix} on the stability of multicomponent solid solution, is defined as [21–23]:

$$\Omega = T_m \Delta S_{mix} / |\Delta H_{mix}| \quad (4)$$

$$T_m = \sum_{i=1}^n x_i T_i \quad (5)$$

$$\Delta H_{mix} = \sum_{i=1, i \neq j}^n \Omega_{ij} c_i c_j \quad (6)$$

where n is the number of elements, x_i is the mole fraction of each element, T_i is the melting temperature of each element, and T_m is the average melting temperature of the n -element alloy. Furthermore, a lower Ω and smaller n improve the glass-forming ability (GFA) of the BMGC [24].

Table 3 shows the atomic radius ratio ψ between the Ce element and the other components of the alloys. The atomic size differences were much larger than 12%, which promoted the formation of a denser and more uniform disordered stacking structure, as well as enhancing the solid–liquid interface energy. As the viscosity of the supercooled liquid increased and made the long-range diffusion of atoms more difficult, the GFA of the alloy was improved [25]

Table 3. Atomic radius ratio ψ between Ce and alloy elements.

Element	Fe	Mn	Si	Cr	C	Ti	Ni	Cu
ψ	1.43	1.38	1.36	1.43	2.12	1.26	1.47	1.42

Figure 3 gives the relationships between phase selection, atomic size difference δ , and ΔH_{mix} . δ is defined as [26]:

$$\delta = \sqrt{\sum_{i=1}^n x_i \left(1 - \frac{d_i}{\sum_{j=1}^n x_j d_j} \right)^2} \quad (7)$$

where d_i and d_j are the atomic diameters of the components i and j , respectively. From Figure 3, the TRIP BMGCs were located in the BMG formation zone, that is, $-40 < \Delta H_{mix} < -5$ kJ/mol, and $6\% < \delta < 18\%$.

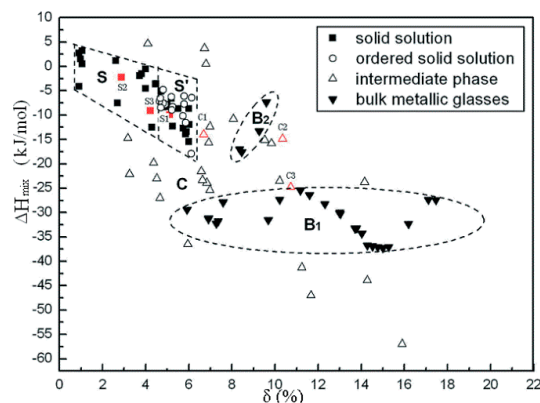


Figure 3. Relationships of phase selection, atomic size difference δ , and mixing enthalpy ΔH_{mix} [26].

Moreover, elemental Ce, which can be used as an oxygen adsorbent, preferentially reacts with residual O in the atmosphere to form a stable compound, thereby purifying the melts and suppressing the heterogeneous nucleation and crystal growth, thus improving their glass forming ability [3,14].

3.2. Mechanical Behaviors of the Fe-Based and Ti-Based TRIP BMGCs

Figure 4 shows the compressive engineering stress–strain curves of Fe-based and Ti-based TRIP BMGCs. All the four alloys exhibited excellent comprehensive mechanical properties, such as the high fracture strength σ_f , large plastic strain ε_p , and excellent work-hardening abilities. From Figure 4a, the fracture strength and plastic strain of $\text{Fe}_{65.4}\text{Mn}_{14.3}\text{Si}_{9.4}\text{Cr}_{10}\text{C}_{0.9}$ BMGC were 2321 MPa and 20.7%, respectively. After adding elemental Ce, the σ_f and ε_p went up to 2905 MPa and 30.1%. Furthermore, the energy stored up to the fracture of the Fe-based BMGCs, found via the integration of the stress versus strain curves, were 511.85 and 725.64 J/m³, respectively. From Figure 4b, the σ_f and ε_p of the Ti-based BMGC significantly improved from the 2006 MPa and 11.3% of $\text{Ti}_{40}\text{Ni}_{40}\text{Cu}_{20}$ to 2635 MPa and 13.8% by adding 1% elemental Ce. Meanwhile, the energy stored up to the fracture of the Ti-based BMGCs improved from 193.22 to 404.49 J/m³.

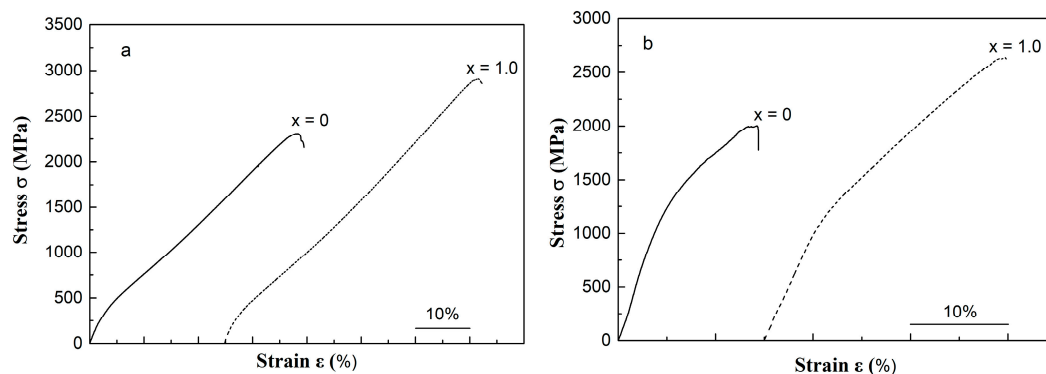


Figure 4. Compressive engineering stress–strain curves of: (a) $\text{Fe}_{65.4-x}\text{Ce}_x\text{Mn}_{14.3}\text{Si}_{9.4}\text{Cr}_{10}\text{C}_{0.9}$ and (b) $\text{Ti}_{40-x}\text{Ce}_x\text{Ni}_{40}\text{Cu}_{20}$ ($x = 0, 1.0$) alloys.

Figure 5 gives the work-hardening rate θ versus the true strain curves for the four BMGCs. The θ can be obtained from $d\sigma_T/d\varepsilon_T$. In the initial stage of deformation, the alloys with no added Ce exhibited a larger θ and smaller yield strength σ_y . Since the elemental Ce contributed to the stabilization of the amorphous matrix, it was difficult to form dislocations when loading. The higher the dislocation density was, the greater the work-hardening rate.

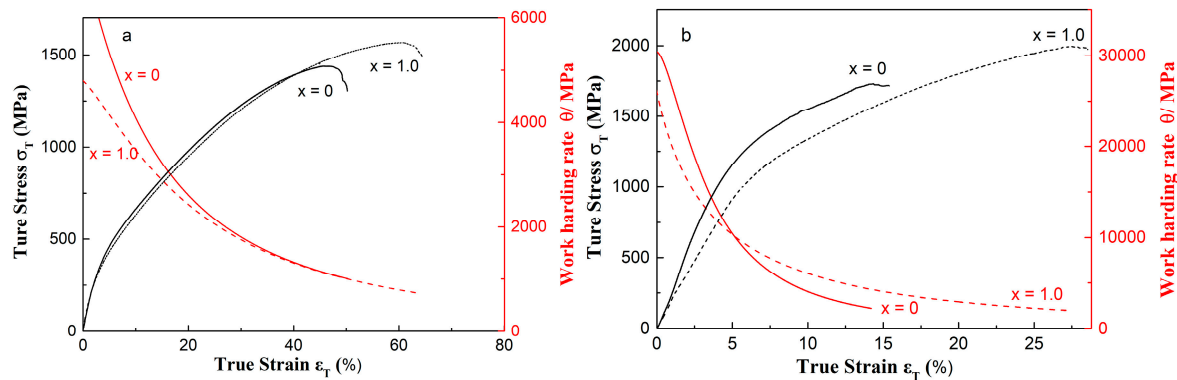


Figure 5. Work-hardening rate and true stress versus true strain curves of: (a) $\text{Fe}_{65.4-x}\text{Ce}_x\text{Mn}_{14.3}\text{Si}_{9.4}\text{Cr}_{10}\text{C}_{0.9}$ and (b) $\text{Ti}_{40-x}\text{Ce}_x\text{Ni}_{40}\text{Cu}_{20}$ ($x = 0, 1.0$) alloys.

From Figure 5a, the θ of Fe-based BMGCs was obviously smaller than that of the Ti-based BMGCs, which was attributed to the different mixed crystal structure. The existence of ferrite reduced the θ of Fe-based BMGCs. As austenite exhibits a higher work-hardening ability than ferrite [27], the TRIP effect dominated the work-hardening behavior of the composites. The alloys with added Ce showed a longer subsequent strengthening and toughening deformation stage. The enhanced GFA significantly delayed the proliferation of dislocations. In the last stage, the two curves nearly coincided. The austenite was almost exhausted by the phase transition, while ferrite played a dominant role.

From Figure 5b, as the GFA improved, Ti-based BMGCs showed a higher work-hardening rate, larger σ_y and smaller ε_p compared with Fe-based alloys. Furthermore, Ce addition decreased the dislocation density and delayed the phase transition process. When the strain was greater than 6%, the work-hardening rate was higher than $\text{Ti}_{40}\text{Ni}_{40}\text{Cu}_{20}$. $\text{Ti}_{39}\text{CeNi}_{40}\text{Cu}_{20}$ and $\text{Fe}_{64.4}\text{CeMn}_{14.3}\text{Si}_{9.4}\text{Cr}_{10}\text{C}_{0.9}$ showed a longer work-hardening period before fracture than the alloys without added Ce. That is, Ce addition further improved the strengthening and toughening effects of TRIP BMGCs.

3.3. Fracture Morphology of the Fe-Based and Ti-Based TRIP BMGCs

Figures 6 and 7 show the fracture morphology of the Fe-based and Ti-based TRIP BMGCs, respectively. The edge regions maintained the disordered structure from the frozen liquid metal due to the high cooling rate. Furthermore, as mentioned, adding elemental Ce can improve the GFA, as well as further develop the densely disordered clusters. As the final fracture occurred, the sudden rise of temperature in the locally softened shear bands led to local melting and thus formed numerous amorphous vein patterns. The densely continuous vein patterns can be seen in Figure 6a,c, and the distribution is more uniform in Figure 6c. From Figure 6b,d, a large quantity of dimples can be seen in the center zone of the Fe-based BMGCs, while the dimple distribution of $\text{Fe}_{64.4}\text{CeMn}_{14.3}\text{Si}_{9.4}\text{Cr}_{10}\text{C}_{0.9}$ is more uniform. Compared with the Fe-based alloys, the veins in the edge region of the Ti-based BMGCs were sparse and developed in a river-like pattern, as well as the dimples in the center zone being relatively shallow. Furthermore, the dimples of the $\text{Ti}_{39}\text{CeNi}_{40}\text{Cu}_{20}$ alloy were also more evenly distributed than without Ce addition.

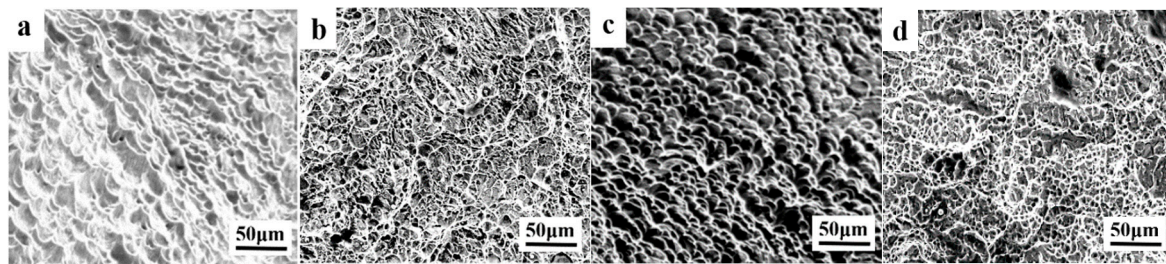


Figure 6. SEM images of the compressive fractured surface of the (a) edge and (b) center of the $\text{Fe}_{65.4}\text{Mn}_{14.3}\text{Si}_{9.4}\text{Cr}_{10}\text{C}_{0.9}$ alloy, and the (c) edge and (d) center of the $\text{Fe}_{64.4}\text{CeMn}_{14.3}\text{Si}_{9.4}\text{Cr}_{10}\text{C}_{0.9}$ alloy.

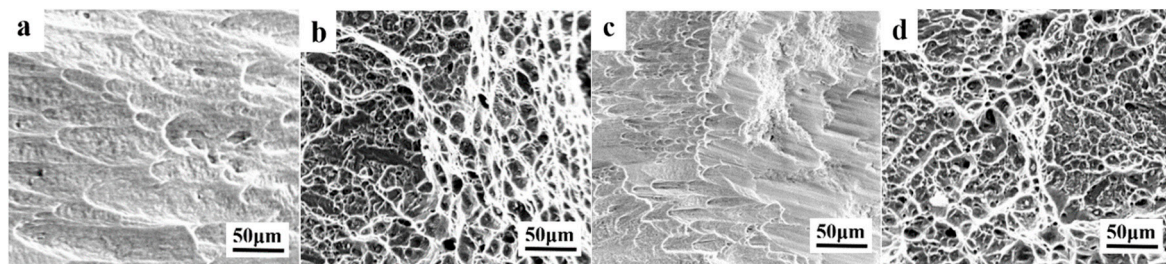


Figure 7. SEM images of the compressive fractured surface of the (a) edge and (b) center of the $\text{Ti}_{40}\text{Ni}_{40}\text{Cu}_{20}$ alloy, and the (c) surface and (d) center of the $\text{Ti}_{39}\text{CeNi}_{40}\text{Cu}_{20}$ alloy.

4. Conclusions

In the present work, we designed the medium-entropy Fe-based and Ti-based BMGCs via shape memory crystalline phase transitions induced plasticity to enhance both their strength and ductility. Adding elemental Ce could stabilize the amorphous phase and enhance the GFA, as well as improve the TRIP effects. The Ce microalloyed BMGCs with larger ΔS_{mix} and δ , and a smaller ΔH_{mix} , exhibited a better GFA, as well as excellent comprehensive mechanical properties. The thermodynamic parameters of the $\text{Fe}_{64.4}\text{CeMn}_{14.3}\text{Si}_{9.4}\text{Cr}_{10}\text{C}_{0.9}$ alloy— ΔS_{mix} , δ , and ΔH_{mix} —changed from 1.05R to 1.08R $\text{J}\cdot\text{mol}^{-1}\cdot\text{K}^{-1}$, 3.69% to 5.62%, and -14.34 to -14.43 $\text{kJ}\cdot\text{mol}^{-1}$, respectively. The σ_f and ε_p went up to 2905 MPa and 30.1%, respectively. For the $\text{Ti}_{39}\text{CeNi}_{40}\text{Cu}_{20}$ alloy, ΔS_{mix} and δ increased from 1.06R to 1.10R and 7.01 to 7.85, respectively. Furthermore, ΔH_{mix} decreased from -23.72 to -24.12 , and the σ_f and ε_p improved to 2635 MPa and 13.8% and 2905 MPa and 30.1%, respectively. The novel TRIP BMGCs can serve as an important guidance for future metastable metals with superior mechanical properties.

Author Contributions: Conceptualization, Y.Z. and W.L.; methodology, Y.Z. and W.L.; validation, Y.Z. and W.L.; formal analysis, Y.Z., P.Z., and J.J.; investigation, Y.Z., P.Z., X.M., and J.J.; resources, Y.Z. and S.K.; data curation, Y.Z., P.Z., X.M., and Z.Y.; writing—original draft preparation, Y.Z. and J.J.; writing—review and editing, W.L.; supervision, W.L.; project administration, Y.Z. and W.L.; funding acquisition, Y.Z. and W.L.

Funding: This research was funded by the National Natural Science Foundation of China, grant number 51661017; Outstanding Youth Funds of Gansu Province of China, grant number 17JR5RA108; and Hongliu Outstanding Talents Program of Lanzhou University of Technology, grant number 2018.

Acknowledgments: We acknowledge Xiaopeng Yuan for insightful discussions.

Conflicts of Interest: All the authors declare no conflicts of interest. The funders had no role in the design of the study; in the collection, analyses, or interpretation of data; in the writing of the manuscript, nor in the decision to publish the results.

References

1. Qiao, J.C.; Wang, Q.; Pelletier, J.M.; Kato, H.; Casalini, R.; Crespo, D.; Pineda, E.; Yao, Y.; Yang, Y. Structural heterogeneities and mechanical behavior of amorphous alloys. *Prog. Mater. Sci.* **2019**, *104*, 250. [[CrossRef](#)]
2. Wang, W.H. Bulk metallic glasses with functional physical properties. *Adv. Mater.* **2009**, *21*, 4524. [[CrossRef](#)]
3. Qiao, J.W.; Jia, H.L.; Liaw, P.K. Metallic glass matrix composites. *Mater. Sci. Eng. R Rep.* **2016**, *100*, 1–69. [[CrossRef](#)]

4. Schuh, C.A.; Hufnagel, T.C.; Ramamurty, U. Mechanical behavior of amorphous alloys. *Acta Mater.* **2007**, *55*, 4067. [[CrossRef](#)]
5. Schroers, J. Processing of bulk metallic glass. *Adv. Mater.* **2010**, *22*, 1566. [[CrossRef](#)] [[PubMed](#)]
6. Lazzara, G.; Cavallaro, G.; Panchal, A.; Fakhrullin, R.; Stavitskaya, A.; Vinokurov, V.; Lvov, Y. An assembly of organic-inorganic composites using halloysite clay nanotubes. *Curr. Opin. Colloid Interface* **2018**, *35*, 42–50. [[CrossRef](#)]
7. Wu, Y.; Ma, D.; Li, Q.K.; Stoica, A.D.; Song, W.L.; Wang, H.; Liu, X.J.; Stoica, G.M.; Wang, G.Y.; An, K. Transformation-induced plasticity in bulk metallic glass composites evidenced by in-situ neutron diffraction. *Acta Mater.* **2017**, *124*, 478–488. [[CrossRef](#)]
8. Pauly, S.; Das, J.; Bednarcik, J.; Mattern, N.; Kim, K.B.; Kim, D.H.; Eckert, J. Deformation-induced martensitic transformation in Cu-Zr-(Al,Ti) bulk metallic glass composites. *Scr. Mater.* **2009**, *60*, 431–434. [[CrossRef](#)]
9. Wu, Y.; Xiao, Y.H.; Chen, G.L.; Liu, C.T.; Lu, Z.P. Bulk metallic glass composite with transformation-mediated work-hardening and ductility. *Adv. Mater.* **2010**, *22*, 2770. [[CrossRef](#)] [[PubMed](#)]
10. Tian, X.; Zhang, K.; Tan, C.; Guo, E. Influence of doping tb on the mechanical properties and martensitic transformation of Ni-Mn-Sn magnetic shape memory alloys. *Crystals* **2018**, *8*, 247. [[CrossRef](#)]
11. Yu, H.B.; Hu, J.; Xia, X.X.; Sun, B.A.; Li, X.X.; Wang, W.H.; Bai, H.Y. Stress-induced structural inhomogeneity and plasticity of bulk metallic glasses. *Scr. Mater.* **2009**, *61*, 640–643. [[CrossRef](#)]
12. Wu, Y.; Wang, H.; Wu, H.H.; Zhang, Z.Y.; Hui, X.D.; Chen, G.L.; Ma, D.; Wang, X.L.; Lu, Z.P. Formation of Cu-Zr-Al bulk metallic glass composites with improved tensile properties. *Acta Mater.* **2011**, *59*, 2928–2936. [[CrossRef](#)]
13. Li, W.; Zhao, C. Microstructure and phase transformation analysis of Ni_{50-x}Ti₅₀La_x shape memory alloys. *Crystals* **2018**, *8*, 345. [[CrossRef](#)]
14. Park, J.M.; Park, J.S.; Na, J.H.; Kim, D.H.; Kim, D.H. Effect of Y addition on thermal stability and the glass forming ability in Fe-Nb-B-Si bulk glassy alloy. *Mater. Sci. Eng. A* **2006**, *435*, 425–428. [[CrossRef](#)]
15. Zhang, J.; Tan, H.; Feng, Y.P. The effect of Y on glass forming ability. *Scr. Mater.* **2005**, *53*, 183. [[CrossRef](#)]
16. Kariper, İ.A. The production of UV absorber amorphous Cerium sulfide thin film. *Mater. Res.* **2017**, *20*, 1345. [[CrossRef](#)]
17. Gaskell, D.R. *Introduction to the Thermodynamics of Materials*, 3rd ed.; Taylor & Francis Ltd.: Washington, DC, USA, 2008; pp. 80–84.
18. Swalin, R.A. *Thermodynamics of Solids*, 2nd ed.; Wiley: New York, NY, USA, 1972; pp. 35–41.
19. Gao, M.C.; Yeh, J.W.; Liaw, P.K.; Zhang, Y. *High-Entropy Alloys: Fundamentals and Applications*, 1st ed.; Springer International Publishing: Cham, Switzerland, 2016.
20. Takeuchi, A.; Inoue, A. Classification of bulk metallic glasses by atomic size difference, heat of mixing and period of constituent elements and its application to characterization of the main alloying element. *Mater. Trans.* **2005**, *46*, 2817–2829. [[CrossRef](#)]
21. Yang, X.; Zhang, Y. Prediction of high-entropy stabilized solid-solution in multicomponent alloys. *Mater. Chem. Phys.* **2012**, *132*, 233–238. [[CrossRef](#)]
22. Zhang, Y.; Yang, X.; Liaw, P.K. Alloy design and properties optimization of high-entropy alloys. *JOM* **2012**, *64*, 830–838. [[CrossRef](#)]
23. Yang, X.; Chen, S.Y.; Cotton, J.D.; Zhang, Y. Phase stability of low-density, multiprincipal component alloys containing aluminum, magnesium, and lithium. *JOM* **2014**, *10*, 2009–2020. [[CrossRef](#)]
24. Zhang, Y.; Lu, Z.P.; Ma, S.G.; Liaw, P.K.; Tang, Z.; Cheng, Y.Q.; Gao, M.C. Guidelines in predicting phase formation of high-entropy alloys. *MRS Commun.* **2014**, *4*, 57–62. [[CrossRef](#)]
25. Wang, W.H.; Dong, C.; Shek, C.H. Bulk metallic glasses. *Mater. Sci. Eng. R Rep.* **2004**, *44*, 45–89. [[CrossRef](#)]
26. Zhang, Y.; Zhou, Y.J.; Lin, J.P.; Chen, G.L.; Liaw, P.K. Solid-solution phase formation rules for multi-component alloys. *Adv. Eng. Mater.* **2008**, *10*, 534–538. [[CrossRef](#)]
27. Hwang, S.W.; Ji, J.H.; Lee, E.G.; Park, K.T. Tensile deformation of a duplex Fe-20Mn-9Al-0.6C steel having the reduced specific weight. *Mater. Sci. Eng. A* **2011**, *528*, 5196–5203. [[CrossRef](#)]

